Journal of Computational Physics **155,** 223–247 (1999)
Article ID jcph.1999.6341, available online at http://www.idealibrary.com on IDEAL®

A Numerical Study of Undulatory Swimming

H. Liu* and K. Kawachi†

**Department of Mechanical and Systems Engineering, Nagoya Institute of Technology, Gokiso-cho, Showa-ku, Nagoya 466, Japan; and †Research Center for Advanced Science and Technology, University of Tokyo, Tokyo 113-8654, Japan*

Received January 27, 1999; revised July 14, 1999

A numerical study of undulatory locomotion is presented. Unsteady hydrodynamics around an undulatory swimming body is solved using a time-accurate solution of the three-dimensional, incompressible, laminar Navier–Stokes equations. A realistic tadpole-shaped body is modeled, which "swims" by sending a laterally compressing, sinusoidal wave down the tail tip. The method is validated by an extensive numerical study of the thrust generation of an oscillating airfoil, involving comparisons with reliable experimental results. For a three-dimensional tadpole model that undergoes undulatory swimming, the hydrodynamics and mechanism of the undulatory swimming were then analyzed and compared with conventional hydrodynamic theories, which provide a general understanding of the relationship between the dynamic vortex flow and the jet-stream propulsion associated with undulatory locomotion of vertebrates.

Key Words: Navier–Stokes equations (unsteady, incompressible); biological fluid mechanics (jet-stream propulsion, undulatory swimming); vorticity flow (reverse von Karman vortex, wake).

INTRODUCTION

In nature, aquatic animals are smart swimmers, using jet-stream propulsion effectively, achieving remarkable propulsive efficiency by comparison to man-made machines. This is a classic fluid problem of undulatory swimming in the form of propagating a transverse wave along the body from head to tail. This swimming, covering a wide range of Reynolds numbers from on the order of 10^2 for tadpole larvae up to on the order of 10^8 for the most rapid cetacean, has been observed to be the most effective movement of swimming propulsion employed by a large number of aquatic animals. Lighthill [1] gave an introduction to the hydrodynamics of aquatic animal propulsion, which elucidated both the zoological and hydromechanical aspects of the subject. Wu [2–4] systematically studied the

0021-9991/99 $30.00

hydrodynamics of swimming propulsion, using linearized inviscid flow theory. Newman [5] applied a slender-body theory to fish-like forms having both thickness and appended lifting surfaces, focusing attention on the case of steady-state motion with a constant angle of attack and induced drag. Lighthill [6] proposed a large-amplitude enlongated-body theory describing in detail how complex fish movement generates thrust and lateral forces to both sides. More recently, Cheng *et al.* [7] developed a three-dimensional waving plate theory pointing out that undulatory motion can reduce three-dimensional effects. These conventional theories are, however, established on a basis of potential flow formulation, linearized body boundary conditions, and an assumed shape for the wake, which can neither solve the nonlinear flow–body interaction nor allow wake dynamics to develop.

Experimentally, recent studies [8–11] of propulsion of oscillating hydrofoils to correlate the relationship between mechanical propulsive efficiency and Strouhal number have provided evidence that optimal efficiency is achieved when a staggered array of reverse Karman vortices is formed in the wake within a narrow range of Strouhal numbers. Triantafyllou *et al.* [9] pointed out that this occurs for most fishes in a range from 0.25 to 035. A study by Triantafyllou and Triantafyllou visualizing the wake behind a robotic tuna [12] further identified the phenomenon in which a clear image of the vortex street was observed within the reported range of the Strouhal number for fish. However, what law of hydrodynamics this thrust-generation mechanism obeys and how the relationship between three-dimensional geometry and swimming mode of a realistic vertebrate affects its propulsion are actually not very clear yet.

We have approached this problem by developing a robust Navier–Stokes (N–S) equation solver [13–15] that can simulate highly unsteady flows around an undulating locomotor that can undergo large-amplitude lateral undulation and has an arbitrary 3D geometry. The validity of the 3D steady simulation was verified by comparison of flow pattern, pressure distribution, and integrated drag with reliable experimental data collected on ship models [13]. The time-accurate reliability was further confirmed in the present study by an extensive study involving grid refinement and by comparison with limited experimental results related to an oscillating hydrofoil.

The dynamic vortex flow–body interaction of undulatory swimming was analyzed by modeling a unique, "nonstreamlined" swimmer—a tadpole that wobbles, normally with the largest lateral inflection at the tail tip twice those commonly observed in most teleost fishes. They have a globose head and body, with a laterally flattened tail abruptly appended to it. Tadpoles swim with large lateral deflections compared with those of normal teleost fishes [16, 17]. Our 3D CFD analysis of tadpole locomotion provides an introduction and overview of the unsteady hydrodynamics of 3D undulatory swimming by vertebrates. Our study specifically confirms that tadpoles swim efficiently, with elegant coupling between their specific kinematics and their unique morphology.

NUMERICAL MODELING OF UNDULATORY SWIMMING

Consider the flow around an undulatory swimming animal with the body moving with respect to a body-fixed reference frame (x, y, z), as depicted in Fig. 1a. A general formulation of the problem is performed in the body-fixed system so that any translational movement of the body can be treated as incoming flow past the body.

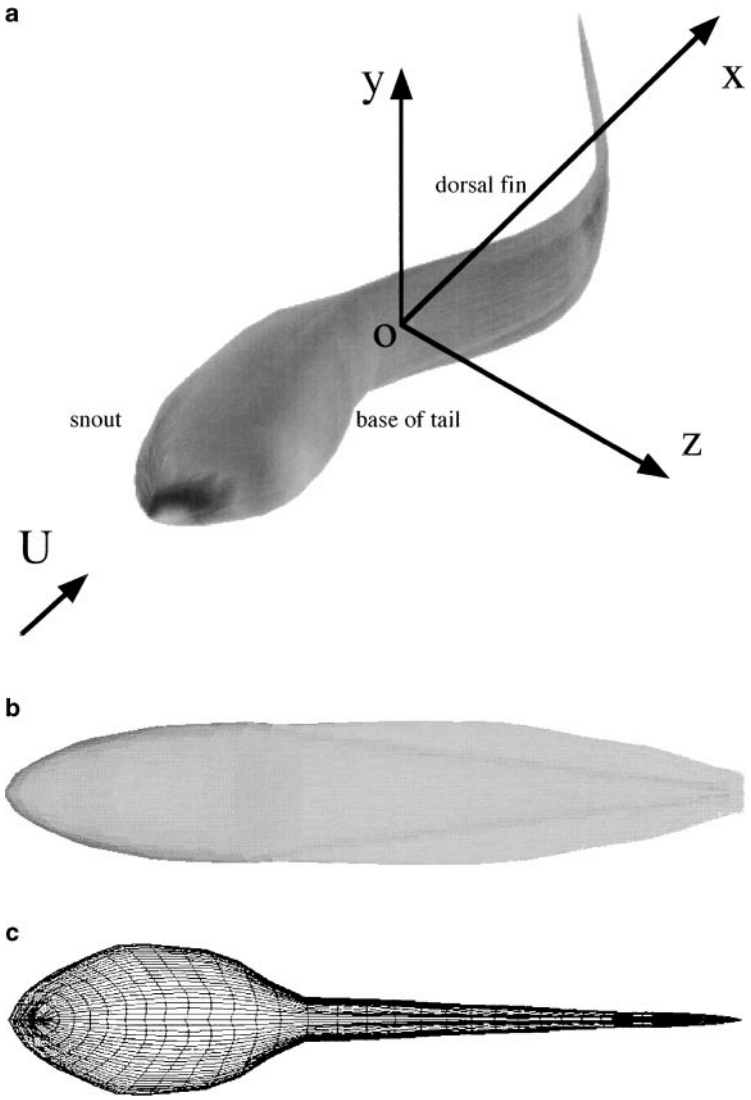

FIG. 1. (a) Definition of the body-fixed system (x, y, z), (b) side view of the tadpole model; and (c) top view of the skeleton of the tadpole model.

Time-Accurate Solution to the Navier–Stokes Equations

Governing Equations

The governing equations are the three-dimensional, incompressible, unsteady Navier–Stokes equations written in strong conservation form for mass and momentum. The artificial compressibility method is used by adding a pseudo time derivative of pressure to the continuity equation. For an arbitrary deformable control volume $V(t)$, i.e., a cell as illustrated in Fig. 2, the nondimensionalized governing equations are

$$\int_{V(t)} \left(\frac{\partial \mathbf{Q}}{\partial t} + \frac{\partial \mathbf{u}_0}{\partial t} + \frac{\partial \mathbf{q}}{\partial \tau} \right) dV + \int_{V(t)} \left(\frac{\partial \mathbf{F}}{\partial x} + \frac{\partial \mathbf{G}}{\partial y} + \frac{\partial \mathbf{H}}{\partial z} + \frac{\partial \mathbf{F}_v}{\partial x} + \frac{\partial \mathbf{G}_v}{\partial y} + \frac{\partial \mathbf{H}_v}{\partial z} \right) dV = 0, \tag{1}$$

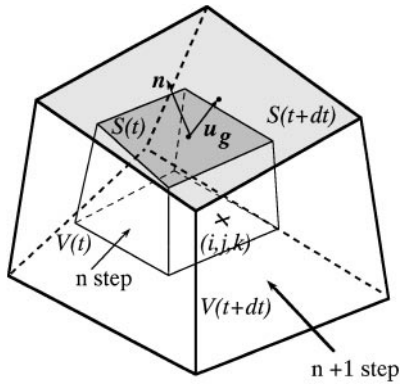

FIG. 2. Layout of the cell-centered control volumes at n and $n+1$ steps.

where

$$\mathbf{Q}=\begin{bmatrix}u\\v\\w\\0\end{bmatrix},\ \mathbf{u}_0=\begin{bmatrix}u_0\\v_0\\w_0\\0\end{bmatrix},\ \mathbf{q}=\begin{bmatrix}u\\v\\w\\p\end{bmatrix},\ \mathbf{F}=\begin{bmatrix}u^2+p\\uv\\uw\\\beta u\end{bmatrix},\ \mathbf{G}=\begin{bmatrix}vu\\v^2+p\\vw\\\beta v\end{bmatrix},\ \mathbf{H}=\begin{bmatrix}wu\\wv\\w^2+p\\\beta w\end{bmatrix},$$

$$\mathbf{F}_v=-\left(\frac{1}{\mathrm{Re}}+\nu_t\right)\begin{bmatrix}2u_x\\u_y+v_x\\u_z+w_x\\0\end{bmatrix},\ \mathbf{G}_v=-\left(\frac{1}{\mathrm{Re}}+\nu_t\right)\begin{bmatrix}v_x+u_y\\2v_y\\v_z+w_y\\0\end{bmatrix},$$

$$\mathbf{H}_v=-\left(\frac{1}{\mathrm{Re}}+\nu_t\right)\begin{bmatrix}w_x+u_z\\w_y+v_z\\2w_z\\0\end{bmatrix}.$$

In the preceding equations, β is the pseudo compressibility coefficient; p is pressure; u, v, and w are velocity components in Cartesian coordinate system x, y, and z; t denotes physical time, and τ is pseudo time. Re is the Reynolds number, and ν_t is the eddy viscosity in turbulence simulation. The term $\mathbf{u}_0$ expresses the velocity vector of the swimming body when undergoing acceleration. Note that the term $\mathbf{q}$ associated with the pseudo time is designed for an inner iteration at each physical time step and will vanish when the divergence of velocity is driven to zero to satisfy the equation of continuity.

By introducing the generalized Reynolds transport theorem and by employing the Gauss integration theorem in the first and second integrals in Eq. (1), respectively, an integrated form of the governing equations in a general curvilinear coordinate system is gained as

$$\int_{V(t)}\left(\frac{\partial\mathbf{u}_0}{\partial t}+\frac{\partial\mathbf{q}}{\partial\tau}\right)dV+\frac{\partial}{\partial t}\int_{V(t)}\mathbf{Q}\,dV+\oint_{S(t)}(\mathbf{f}-\mathbf{Q}\mathbf{u}_g)\cdot\mathbf{n}d=0, \tag{2}$$

where $\mathbf{f}=(\mathbf{F}+\mathbf{F}_v,\mathbf{G}+\mathbf{G}_v,\mathbf{H}+\mathbf{H}_v)$; $S(t)$ denotes the surface of the control volume; n_x, n_y, and n_z are components of the unit outward normal vector ($\mathbf{n}$) corresponding to all the faces of the polyhedron cell; and $\mathbf{u}_g$ is the local velocity of the moving cell surface (see Fig. 2).

The relationship between the physical and computational spaces is given as

$$\begin{cases} \xi = \xi(x, y, z, t) \\ \eta = \eta(x, y, z, t) \\ \zeta = \zeta(x, y, z, t) \\ t^* = t \end{cases} \longleftrightarrow \begin{cases} x = x(\xi, \eta, \zeta, t^*) \\ y = y(\xi, \eta, \zeta, t^*) \\ z = z(\xi, \eta, \zeta, t^*) \\ t = t^* \end{cases} \tag{3}$$

where t^* denotes the time in computational space (ξ, η, ζ). The last term in Eq. (2) expresses the net flux across the cell faces. For a structured, boundary-fitted, and cell-centered storage architecture, we can further reform Eq. (2) in terms of the semi-discrete form, where (i, j, k) denote the cell index (see Fig. 2), such that

$$\frac{\partial}{\partial t}[V\mathbf{Q}]_{ijk} + \mathbf{R}_{ijk} + V_{ijk}\left(\mathbf{a}_0 + \frac{\partial \mathbf{q}}{\partial \tau}\right)_{ijk} = 0, \tag{4}$$

where

$$\begin{aligned} \mathbf{R}_{ijk} = {} & (\hat{\mathbf{F}} + \hat{\mathbf{F}}_v)_{i+1/2,j,k} - (\hat{\mathbf{F}} + \hat{\mathbf{F}}_v)_{i-1/2,j,k} + (\hat{\mathbf{G}} + \hat{\mathbf{G}}_v)_{i,j+1/2,k} - (\hat{\mathbf{G}} + \hat{\mathbf{G}}_v)_{i,j-1/2,k} \\ & + (\hat{\mathbf{H}} + \hat{\mathbf{H}}_v)_{i,j,k+1/2} - (\hat{\mathbf{H}} + \hat{\mathbf{H}}_v)_{i,j,k-1/2}, \qquad \text{e.g., } \hat{\mathbf{F}} + \hat{\mathbf{F}}_v = (\mathbf{f} - \mathbf{Q}\mathbf{u}_g) \cdot \mathbf{S}_n^{\xi}, \end{aligned}$$

$$\mathbf{S}_n^{\xi} = \left[S_{nx}^{\xi}, S_{ny}^{\xi}, S_{nz}^{\xi}\right], \qquad \mathbf{n} = \left[S_{nx}^{\xi}, S_{ny}^{\xi}, S_{nz}^{\xi}\right]/S, \qquad S = \sqrt{S_{nx}^{\xi^2} + S_{ny}^{\xi^2} + S_{nz}^{\xi^2}}.$$

The term $\mathbf{a}_0$ denotes the acceleration effect (inertia force) of the body which is explicitly derived from the velocity $\mathbf{u}_0$. The term V_{ijk} is the volume of the cell (i, j, k). Note that the unit outward normal vector $\mathbf{n}$ can be calculated using the areas of the cell faces, e.g., $\mathbf{S}_n^{\xi}$ in the ξ-direction (see Fig. 2). A detailed description of the evaluation of the inviscid flux and the viscous flux can be found in Appendixes II and III.

Implicit Algorithm for Time Integration

The Padé scheme is employed for the time integration,

$$\frac{\partial}{\partial t} = \frac{1}{\Delta t}\frac{\Delta}{1 + \theta\Delta}, \quad \text{or} \quad \frac{\Delta(V\mathbf{Q})_{ijk}^{(n+1)} - \Delta(V\mathbf{Q})_{ijk}^{(n)}}{\Delta t} = -\left\{\mathbf{R}_{ijk} + V_{ijk}\left(\mathbf{a}_0 + \frac{\partial \mathbf{q}}{\partial \tau}\right)_{ijk}\right\}^{(n+1)}, \tag{5}$$

where the parameter θ is taken to be 1 for the implicit Euler scheme with first-order accuracy in time; Δt is the time increment; and $\Delta\mathbf{q}^{(n)} = \mathbf{q}^{(n+1)} - \mathbf{q}^{(n)}$. Thus, Eq. (4) can be discretized by replacing the time-related term with Eq. (5), such that

$$\Delta(V\mathbf{Q})_{ijk}^{(n)} + \theta\Delta t\Delta\left[\mathbf{R}_{ijk} + V_{ijk}\left(\mathbf{a}_0 + \frac{\partial \mathbf{q}}{\partial \tau}\right)_{ijk}\right]^{(n)} = -\Delta t\left[\mathbf{R}_{ijk} + V_{ijk}\left(\mathbf{a}_0 + \frac{\partial \mathbf{q}}{\partial \tau}\right)_{ijk}\right]^{(n)}. \tag{6}$$

Since the volume of the cell may change with time due to the moving grid system, we assess the first term in Eq. (6) as

$$\begin{aligned} \Delta(V\mathbf{Q})_{ijk}^{(n)} &= (V\mathbf{Q})_{ijk}^{(n+1)} - (V\mathbf{Q})_{ijk}^{(n)} = V_{ijk}^{(n+1)}\Delta\mathbf{Q}_{ijk}^{(n)} + \Delta V_{ijk}^{(n)}\mathbf{Q}_{ijk}^{(n)} \\ &\approx V_{ijk}^{(n)}\Delta\mathbf{Q}_{ijk}^{(n)} + \Delta V_{ijk}^{(n)}\mathbf{Q}_{ijk}^{(n)}. \end{aligned} \tag{7}$$

A problem rises here as to how to satisfy the so-called "Geometric Conservation Law" (GCL) [18], i.e., the conservation of momentum taken into the Newtonian laws at each time step in terms of evaluation of the increment of the volume $\Delta V_{ijk}^{(n)}$ for the moving grid system. Considering the conservation of flux across the cell faces in an extreme case of solving uniform flow with the moving grid system, $\Delta V_{ijk}^{(n)}$ can be explicitly expressed by substituting Eq. (7) into Eq. (6),

$$\begin{aligned}\Delta V_{ijk}^{(n)} = \Delta t\big[&\left(\mathbf{u}_g \cdot \mathbf{S}_n^{\xi}\right)_{i+1/2} - \left(\mathbf{u}_g \cdot \mathbf{S}_n^{\xi}\right)_{i-1/2} + \left(\mathbf{u}_g \cdot \mathbf{S}_n^{\eta}\right)_{j+1/2} \\ &- \left(\mathbf{u}_g \cdot \mathbf{S}_n^{\eta}\right)_{j-1/2} + \left(\mathbf{u}_g \cdot \mathbf{S}_n^{\zeta}\right)_{k+1/2} - \left(\mathbf{u}_g \cdot \mathbf{S}_n^{\zeta}\right)_{k-1/2}\big]. \end{aligned} \tag{8}$$

With regard to the inertial forces due to the body movements, combining the two terms associated with the acceleration $\mathbf{a}_0$ gives

$$\theta \Delta t \Delta (V_{ijk}\mathbf{a}_0)^{(n)} + \Delta t (V_{ijk}\mathbf{a}_0)^{(n)} = \Delta t\big[(1-\theta)(V_{ijk}\mathbf{a}_0)^{(n)} + \theta V_{ijk}^{(n)}\mathbf{a}_0^{(n+1)}\big]. \tag{9}$$

The pseudo time-related terms designed for the inner iteration can be approximated as

$$\begin{aligned}\theta \Delta t \Delta\left(V_{ijk}\frac{\partial \mathbf{q}}{\partial \tau}\right)^{(n)} + \Delta t\left(V_{ijk}\frac{\partial \mathbf{q}}{\partial \tau}\right)^{(n)} &= \Delta t\left[(1-\theta)\left(V_{ijk}\frac{\partial \mathbf{q}}{\partial \tau}\right)^{(n)} + \theta V_{ijk}^{(n)}\frac{\partial \mathbf{q}^{(n+1)}}{\partial \tau}\right] \\ &\approx \Delta t V_{ijk}^{(n)}\frac{\partial \mathbf{q}^{(n)}}{\partial \tau}. \end{aligned} \tag{10}$$

Note that, in the preceding Eq. (10), the approximation $(\partial \mathbf{q}^{(n)}/\partial\tau = \partial \mathbf{q}^{(n+1)}/\partial\tau)$ is reasonable because the pseudo time τ is for the inner iteration and thus is dependent at each physical time step. Hence, the governing equations become

$$\frac{\Delta \mathbf{Q}_{ijk}^{(n)}}{\Delta t} + \frac{\theta \Delta \mathbf{R}_{ijk}^{(n)}}{V_{ijk}^{(n)}} + \frac{\partial \mathbf{q}^{(n)}}{\partial \tau} = -\frac{\mathbf{R}_{ijk}^{(n)}}{V_{ijk}^{(n)}} - \frac{\Delta V_{ijk}^{(n)}}{\Delta t V_{ijk}^{(n)}}\mathbf{Q}_{ijk}^{(n)} + \big[(1-\theta)\mathbf{a}_{ijk}^{(n)} + \theta \mathbf{a}_{ijk}^{(n+1)}\big]. \tag{11}$$

Pseudo Time Integration for the Inner Iteration

The implicit Euler scheme is also employed (see Eq. (5)) for the pseudo time integration. Note that there exists a special relationship between $\mathbf{Q}_{ijk}^{(n)}$ and $\mathbf{q}_{ijk}^{(n)}$ based on Eq. (1),

$$\mathbf{Q}_{ijk}^{(n,m)} = \mathbf{I}_a \mathbf{q}_{ijk}^{(n,m)}, \qquad \Delta \mathbf{Q}_{ijk}^{(n,m)} = \mathbf{I}_a \mathbf{q}_{ijk}^{(n,m)} - \mathbf{I}_a \mathbf{q}_{ijk}^{(n,0)}, \tag{12}$$

where $\mathbf{I}_a = [1, 1, 1, 0]^{\mathrm{T}}$. Superscript m denotes the number of the inner iteration. With the differencing operator for the pseudo time, the governing equations can be reformulated as

$$\begin{aligned}&\left\{\frac{\mathbf{I}}{\Delta \tau} + \theta\frac{\mathbf{I}_a}{\Delta t}\left(1 + \frac{\Delta V_{ijk}^{(n)}}{V_{ijk}^{(n)}}\right) + \frac{\theta}{V_{ijk}^{(n)}}\frac{\partial \mathbf{R}_{ijk}^{(n,m)}}{\partial q}\right\}\Delta \mathbf{q}_{ijk}^{(n,m)} \\ &= -\frac{1}{V_{ijk}^{(n)}}\big[(1-\theta)\mathbf{R}_{ijk}^{(n)} + \theta \mathbf{R}_{ijk}^{(n,m)}\big] + \frac{\mathbf{I}_a}{\Delta t}\left\{\left(\mathbf{q}_{ijk}^{(n,0)} - \mathbf{q}_{ijk}^{(n,m)}\right) - \frac{\Delta V_{ijk}^{(n)}}{V_{ijk}^{(n)}}\mathbf{q}_{ijk}^{(n,m)}\right\} \\ &\quad + \big[(1-\theta)\mathbf{a}_{ijk}^{(n)} + \theta \mathbf{a}_{ijk}^{(n+1)}\big], \end{aligned} \tag{13}$$

where $\Delta\tau$ is the pseudo time step size. In order to benefit from both lower memory and computational requirements for the solution of Eq. (13), the approximated factorization method of Beam and Warming [19] is used for the LHS, and hence, Eq. (13) is rewritten as

$$\left\{\mathbf{I}+\frac{\theta\Delta t\mathbf{I}_t}{V_{ijk}^{(n)}}\frac{\partial\mathbf{R}_{ijk}^{(n,m)}}{\partial\mathbf{q}}\right\}^{(\xi)}\left\{\mathbf{I}+\frac{\theta\Delta t\mathbf{I}_t}{V_{ijk}^{(n)}}\frac{\partial\mathbf{R}_{ijk}^{(n,m)}}{\partial\mathbf{q}}\right\}^{(\eta)}\left\{\mathbf{I}+\frac{\theta\Delta t\mathbf{I}_t}{V_{ijk}^{(n)}}\frac{\partial\mathbf{R}_{ijk}^{(n,m)}}{\partial\mathbf{q}}\right\}^{(\zeta)}\Delta\mathbf{q}_{ijk}^{(n,m)}$$
$$=-\frac{\Delta t\mathbf{I}_t}{V_{ijk}^{(n)}}\left[(1-\theta)\mathbf{R}_{ijk}^{(n)}+\theta\mathbf{R}_{ijk}^{(n,m)}\right]+\mathbf{I}_t\mathbf{I}_a\left\{\left(\mathbf{q}_{ijk}^{(n,0)}-\mathbf{q}_{ijk}^{(n,m)}\right)-\frac{\Delta V_{ijk}^{(n)}}{V_{ijk}^{(n)}}\mathbf{q}_{ijk}^{(n,m)}\right\}$$
$$+\Delta t\mathbf{I}_t\left[(1-\theta)\mathbf{a}_{ijk}^{(n)}+\theta\mathbf{a}_{ijk}^{(n+1)}\right], \tag{14}$$

where $\mathbf{I}_t=\mathbf{I}/(\theta+\Delta t/\Delta\tau)$, and $\mathbf{I}$ is a unit matrix. The term associated with the change of volume of the LHS is neglected, which does not affect the accuracy of solution when it converges. Note that taking an infinity pseudo time step $\Delta\tau$ reduces the $\mathbf{I}_t$ to a unit matrix. Numerical investigation by Roger *et al.* [20] suggested that this can accelerate the convergence of the inner iteration. The preceding equations can be further decomposed into three sweeps in the ξ-, η-, and ζ-directions in the computational domain. A linear system of equations is finally yielded, in which the discrete form of the matrix from the LHS is tridiagonally banded.

The Kinematic Model

The kinematics for undulatory swimming is based on the straightforward locomotion of a *Rana catesbeiana* larva [16]. A 3D tadpole model was established in which the tadpole could swim under two basic assumptions: (1) the lateral traveling wave is 1D at each cross section without streamwise twisting (like a waving plate) and propagates down the body toward the tail tip, and (2) the body elongates during undulatory swimming. We defined a sinusoidal function to "swim" our tadpole, which is one based on the longitudinal coordinates (Fig. 1) and sends a traveling wave propagating. The wave is of the form

$$z_i=h_i(x,t)=a_i(x)\sin\left[2\pi\left(\frac{x}{\lambda}-\frac{t}{T}\right)\right], \tag{15}$$

where $a_i(x)$ represents amplitude, λ is wavelength, T is period, $h_i(x,t)$ denotes the center plane of the tadpole model, t is time, and x is the coordinate in the x-direction corresponding to the body length. Equation (15) involves, if extended in Fourier series, the first two terms, which is coincidentally similar to an equation developed by Videler [17] for swimming fishes. Videler, however, developed his formula using the first three odd Fourier terms, but pointed out that the contributions of the higher frequencies, even the third and the fifth, were marginal. The present definition of the traveling wave can in principle be extended, by taking the y-coordinate in Eq. (15) into consideration, to mimic full 3D movements of an undulatory swimming animal capable of moving in all three (x, y, and z) planes. Following Liu *et al.* [15], the amplitudes of $a_i(x)$, as illustrated in Fig. 3, are determined by using the spline interpolation from five original maximum amplitudes, a_i, along the length, L, of the tadpole, taken directly from Fig. 3 in [16]. These values are at the snout, $x=0$, $a=0.05L$;

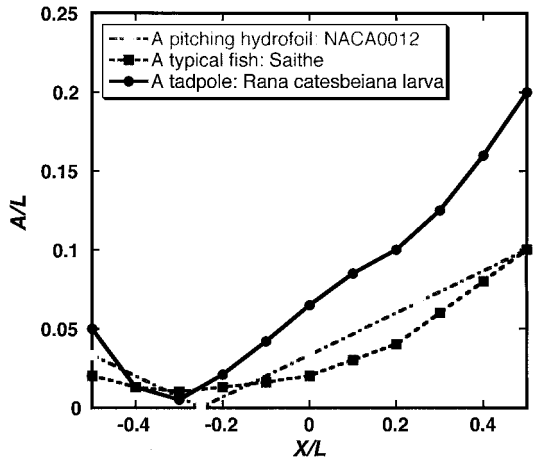

FIG. 3. Maximum amplitudes of the lateral deflection along the body length.

at the otic capsule, $x = 0.19L$, $a = 0.005L$; at the base of the tail, $x = 0.384L$, $a = 0.04L$; at the mid tail, $x = 0.692L$, $a = 0.1L$; and at the tail tip, $x = 1.0L$, $a = 0.2L$. (See Fig. 4.)

Given a reference length L which represents body length and a reference velocity U that is the forward velocity, the Reynolds number (Re) is defined by

$$\mathrm{Re} = \frac{UL}{\nu}, \tag{16}$$

where ν is water viscosity, with a value of 1.533×10^{-6} m^2/s. For the bullfrog tadpole, *R. catesbeiana*, with a body length of 4.7 cm, and a common forward swimming speed of 5 L s^{-1}, the Re is evaluated to be around 7200. Furthermore, by introducing a reduced frequency of $k = 2\pi f L/2U$, where f is frequency, we can reformulate Eq. (15) in the simplified form

$$h_i(x, t) = a_i(x) \sin\left[2\pi\left(\frac{x}{\lambda}\right) - 2kt\right]. \tag{17}$$

Subscript i denotes the grid points of the center line on the center plane. The reduced frequency is evaluated to be 5.843 corresponding to a forward swimming speed of 5 L s^{-1}, from a plot of forward velocity against tail-beat frequency in the study of Wassersug and Hoff [16]. The overall propulsive wavelength is taken as $0.84L$, on the basis of empirical data of $0.84 \pm 0.1L$. Note that in this model the tadpole could swim more like other aquatic vertebrates, including various fishes, by appropriate modifications to the parameters of wavelength, reduced frequency, and the amplitudes of the propulsive wave at five or more points along the length of the animal.

Geometric Model and Grid System

We defined the geometry of the tadpole model on the basis of side and top views of the bullfrog *R. catesbeiana* so that the digitized views are as illustrated in Figs. 1b and lc. A method that can determine 3D geometry using two 2D images of the object based on two pictures of side and top views was developed. Note that most aquatic undulating

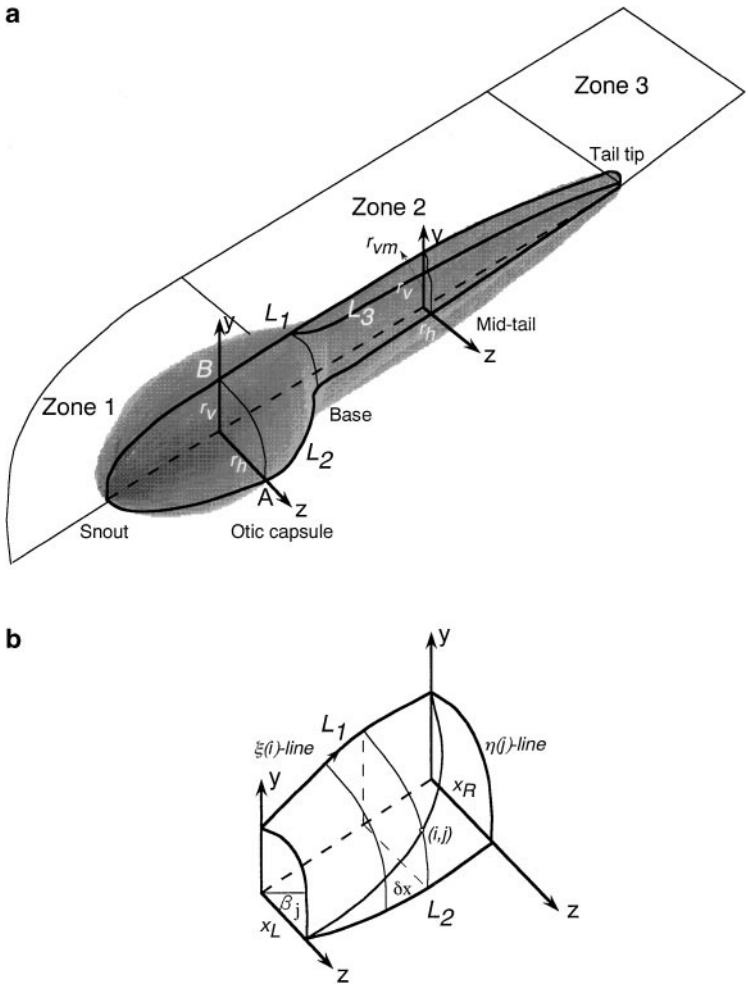

FIG. 4. Schematic diagram of the 3D tadpole model and the computational domain: (a) digitized 3D tadpole body and multi-block zones and (b) grid generation on the tadpole body surface.

swimmers are structurally developed to be smooth bodies of revolution if we think of fins as appendages attached to the body. This implies that using a smooth analytical function to define the outline, namely, the 2D shape for each cross section down the body, can give a good approximation to the overall 3D geometry of the object. Here the problem turns out to be how to accurately determine the 2D shape at each cross section. For simplicity, we consider the tadpole model to have a symmetrical horizontal plane, which will reduce our computing time in half. Tadpoles normally swim by compressing their tails laterally with less vertical motion, which means that a slight discrepancy in the geometry between upper and lower portions seldom leads to a significant vertical force. Thus, the tadpole can swim by staying in the water basically with the help of buoyancy.

We consider that the outline of each section for the tadpole can be well approximated by an elliptic curve as illustrated in Fig. 4a in which two axes of the elliptic curve, r_h and r_v, are determined by two points A and B which are given by the two curves L_1 of the dorsal line and L_2 of the body line on the horizontal plane. We use the side view picture to define the dorsal line L_1, and the top view picture for the horizontal body line L_2. Note that for

the tail of the tadpole we have both a dorsal fin and a dorsal muscle portion, which are of different thickness. We herein introduce two elliptic curves as illustrated in Fig. 4a to match both the dorsal fin and the dorsal muscle of the tail, where another curve L_3 (Fig. 4a) is defined based on the side view image of the tadpole. Based on the fact that the dorsal fin is commonly observed to be roughly a third of the dorsal muscle portion in thickness, we first define an elliptic curve to match the dorsal fin with one axis of $r/3$ and the other of $r_v - r_{vm}$, the difference in height between the dorsal fin and the dorsal muscle portion; and second we make an elliptic curve to fit the dorsal muscle portion with $2r_h/3$ and r_{vm}. Hence, the two elliptic curves can be connected continuously but with a local curvature jump at the joint C. Note that the more points are taken in the longitudinal direction, the better image of the 3D geometry can be gained. As a result, we can construct a complete 3D geometry of the object, with half based on the realistic images and half given analytically. Additionally, a more complicated function can easily be introduced to match the local 2D shape at each section for the complicated geometry of the object.

With consideration of the complicated geometries of tadpoles as well as fishes, we employ a C–O type grid topology as well as a multi-block grid system as illustrated in Fig. 5. Utilization of the C–O type grid topology is capable of closely and smoothly matching the chordwise lines of the body of revolution (i.e., the O-type at each section), particularly at the two ends, and is also efficient in resolving the boundary layer and vortex on the body surface of the posterior tail and especially in the wake (i.e., the C-type). Also, the C–O type grid

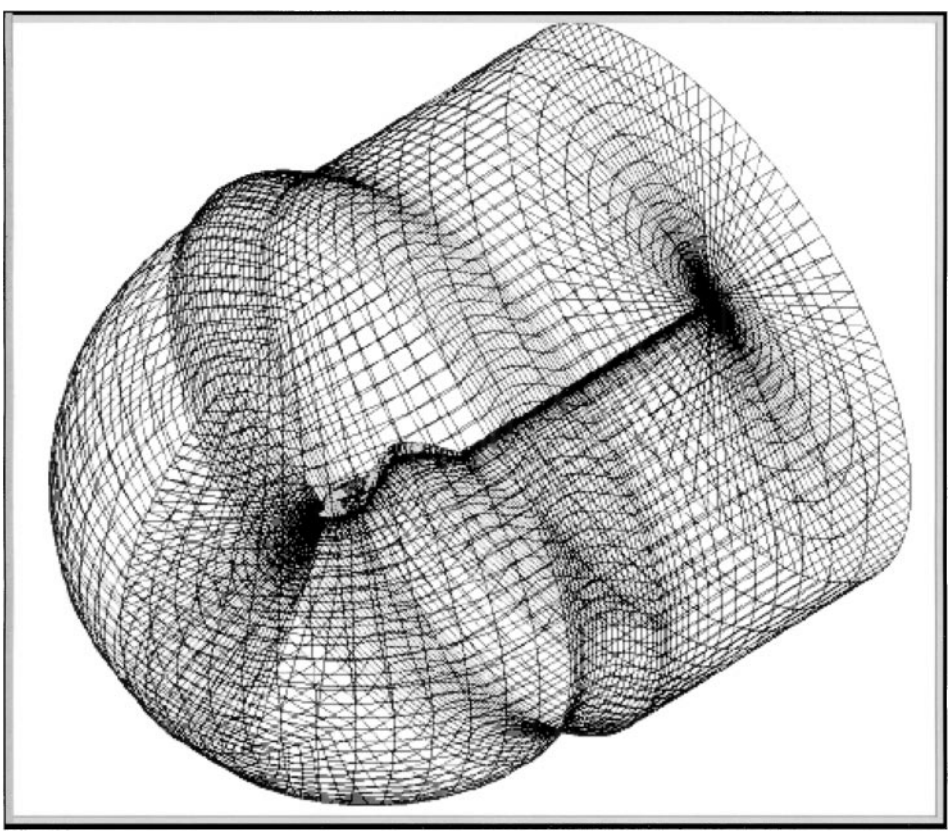

FIG. 5. C–O type grid topology system around an undulatory swimming tadpole.

system appears to be convenient for regenerating grids when the body performs undulating swimming locomotion such that regridding according to some simple rule at each time step can be achieved and hence leads to a large reduction in computing time. To generate high-quality grids corresponding to each portion of the complicated geometry of an aquatic undulating locomotor, a multi-block grid system is herein introduced. For grids around a 3D tadpole-shaped body, taking into consideration the special geometry with a globose head and body and a tapered tail, we divided the domain into three blocks, corresponding to the head and body, the tail, and the wake, respectively. (Details can be found in Appendix IV.)

Boundary Conditions

The computational domain as shown in Fig. 5 consists of the body surface and the upstream and the downstream boundaries. Upstream the velocity components are fixed to be uniform, i.e., $u = 1$ and $v = w = 0$, while pressure is set to zero. Downstream a zero-gradient condition is taken for both velocity and pressure; i.e., $\partial(u, v, w, p)/\partial\xi = 0$. On the tadpole body surface, the no-slip condition is used for the velocity components. To incorporate the dynamic effect due to the acceleration of the oscillating body, pressure divergence at the surface stencils is derived from the local momentum equation, such that

$$\begin{aligned} u &= u_{\text{sw}} \\ \partial p/\partial \text{n} &= -a_0 \cdot n, \end{aligned} \tag{18}$$

where the velocity and the acceleration on the solid wall are evaluated and updated using the renewed grids on the tadpole body surface at each time step. The viscous-related term is negligibly small compared with the inertial forces.

Evaluation of Thrust, Power, and Propulsive Efficiency

The three force components (F_x, F_y, F_z) exerted on the body surface are evaluated by a summation of inviscid and viscous flux over the body surface as

$$F_{\text{body}} = \begin{bmatrix} F_x \\ F_y \\ F_z \\ Q \end{bmatrix} = -\sum_{i}^{\text{body}} (\text{Flux}_{\text{inviscid}} + \text{Flux}_{\text{viscous}}). \tag{19}$$

Note that the fourth component Q comes from the equation of mass conservation as shown in Eq. (1). Thus, the thrust can be defined as an opposite force acting toward the direction of fluid flow, namely, $-F_x$. The power required for the undulating swimming, i.e., the work done in unit time, can be considered a summation of work done by inertial forces and hydrodynamic forces on the body surface such that

$$\begin{aligned} \text{Power} &= \int_{V(t)} \mathbf{F}_z w \, dV = \int_{V(t)} (\rho \ddot{h}(x,t) - F_z) w \, dV \\ &= \int_0^L \rho A(x) \dot{h}(x,t) \ddot{h}(x,t) \, dx - \oint_{S(t)} F_z \dot{h}(x,t) \, dS \\ &\approx \sum_{\text{snout}}^{\text{tail tip}} \rho A_i(x) \dot{h}_i(x,t) \ddot{h}_i(x,t) \Delta x - \sum_{ij}^{\text{body surface}} F_{zi} \dot{h}_i(x,t) \Delta S_{ij}, \end{aligned} \tag{20}$$

where ρ is the water density; $A(x)$ denotes the area of section i on the center plane; and S_{ij} expresses the body surface. Note that the work done in the x- and y-directions is not taken into account in the preceding Eq. (20) because there is no movement in the two directions. Any contribution of bending moment is neglected here. To define the mechanical propulsive efficiency, i.e., the rate of effective work done, in assessing the performance of an undulating swimmer, we define the propulsive efficiency in a time-averaged manner, such that

$$\eta = \frac{C_{\mathrm{T\,ave}} \cdot U}{C_{\mathrm{P\,ave}}}, \tag{21}$$

where, instead of the thrust and power, the dimensionless mean coefficients of C_{T} and C_{P} as defined in Appendix I are used. To facilitate comparison with conventional theories, the thrust here is defined as a contribution from the pressure force while the drag is due to the skin friction. In a sense, we could use another definition by taking the net thrust with the force due to skin friction instead of considering the undulating body overall as a propeller, but that would result in zero efficiency at steadily swimming locomotion.

VALIDATION TEST OF THE METHOD

A variety of validation tests were undertaken [13–15, 21] to assess the reliability of the present methodology and code. A study of the von Karman vortex street in the wake behind a circular cylinder at Reynolds numbers of 105 and 200 was very well captured compared with reported experimental results [13], where the computed Strouhal number of 0.156 was calculated in excellent agreement with the experimental results of the reported values of approximately 0.16.

Note that fluid flows in the following simulations are assumed to be laminar and the eddy viscosity ν_{t} for turbulence simulation is taken to be zero for all the simulations.

Jet-Stream Generation of an Oscillating Foil

To elucidate the mechanism of a jet-like vortex pattern corresponding to a thrust-generating body as described by von Karman and Burgers [22], flows past an NACA0012 airfoil pitching in a uniform flow at Reynolds numbers 1.2×10^4 and 7200 were numerically analyzed. The foil is placed in a body-centered inertial frame of reference that pitches in a sinusoidal form about the quarter-chord point with an amplitude of $0.1L$ (L, chord length) at the trailing edge (corresponding to a pitching angle of approximately 7.75°) in the uniform free stream. Thus, the rigid, nondeforming grid system is allowed to roll with the body through general coordinate transformation, which eliminates the need for generating multiple grids. An extensive grid refinement study was performed and indicated the achievement of highly accurate solutions. An O-type 141×57 grid system was eventually employed, with a minimum grid spacing of approximately 0.001 adjacent to the wall. To identify the optimal thrust generation in transverse oscillation, the Strouhal number ($\mathrm{St} = fA/U$), defined as the production of oscillating frequency (f) multiplied by the width of the wake, i.e., the maximum excursion of the foil's trailing edge (double amplitude, $2A = 0.2L$), divided by the forward speed (U), was taken to vary from 0.0 up to 0.4 with an increment of 0.05. Correspondingly, the reduced frequencies (k) are 0.0, 0.785, 1.571, 2.356, 3.141, 3.927, 4.712, 5.497, and 6.282. The influence of the time step on the computed force-related quantities was validated by testing three time steps of 0.00125, 0.0025, and 0.005, which showed insensitivity of the computed results to the selected time step. The parameter β with

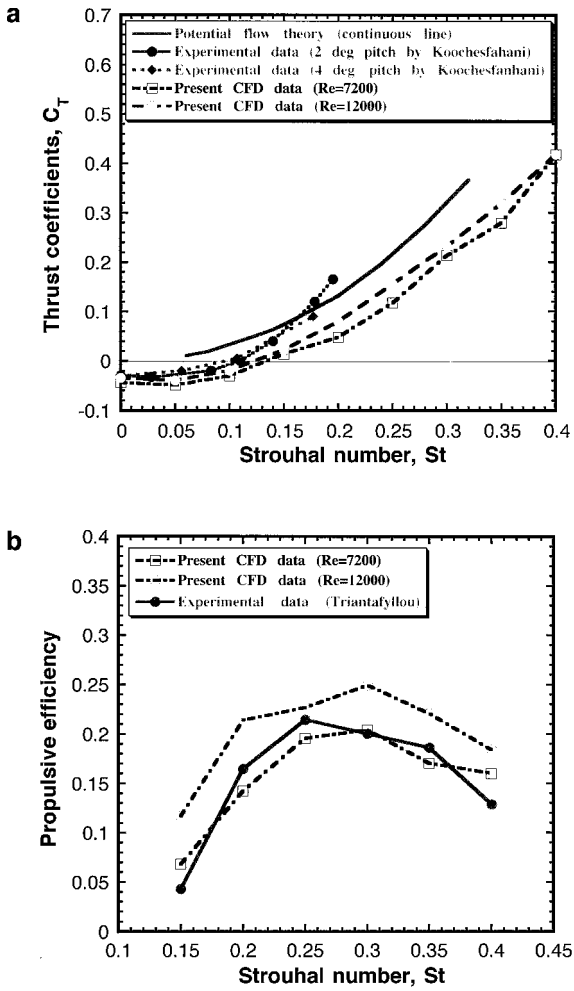

FIG. 6. Mean thrust coefficients C_T and propulsive efficiencies η against Strouhal numbers St of an oscillating airfoil NACA0012 ($\mathrm{Re} = 1.2 \times 10^4$ and $\mathrm{Re} = 7200$): (a) C_T vs St and (b) η vs St.

a value of 50 was employed for all cases, resulting in very fast convergence of the inner iteration with an averaged iterative number $N_{it} = 10$–20 when the divergence of velocity at each time step was taken to be less than 0.05.

The averaged thrust coefficients and the propulsive efficiencies against the Strouhal numbers are plotted in Figs. 6a and 6b and compared with experimental results [8, 9] as well as the potential flow theory. By means of the momentum theory, Koochesfahani [8] used the measured mean velocity profile in the wake (one chord length from the trailing edge: $x/L = 1.0$) to estimate the mean thrust coefficient at Reynolds number 1.2×10^4 without consideration of the contributions due to the fluctuating quantities and the pressure term. Overall, the computed force-related coefficients match very well the tendency of the experimental results in terms of both the thrust and the propulsive efficiency, although a slight discrepancy among different pitching amplitudes as well as in the dependence on Reynolds number is observed. Both thrust and propulsive efficiency show an increase more or less with increasing Reynolds numbers. The propulsive efficiency show an optimal variation against the Strouhal number, with the maximum between 0.25 and 0.35, which is in excellent

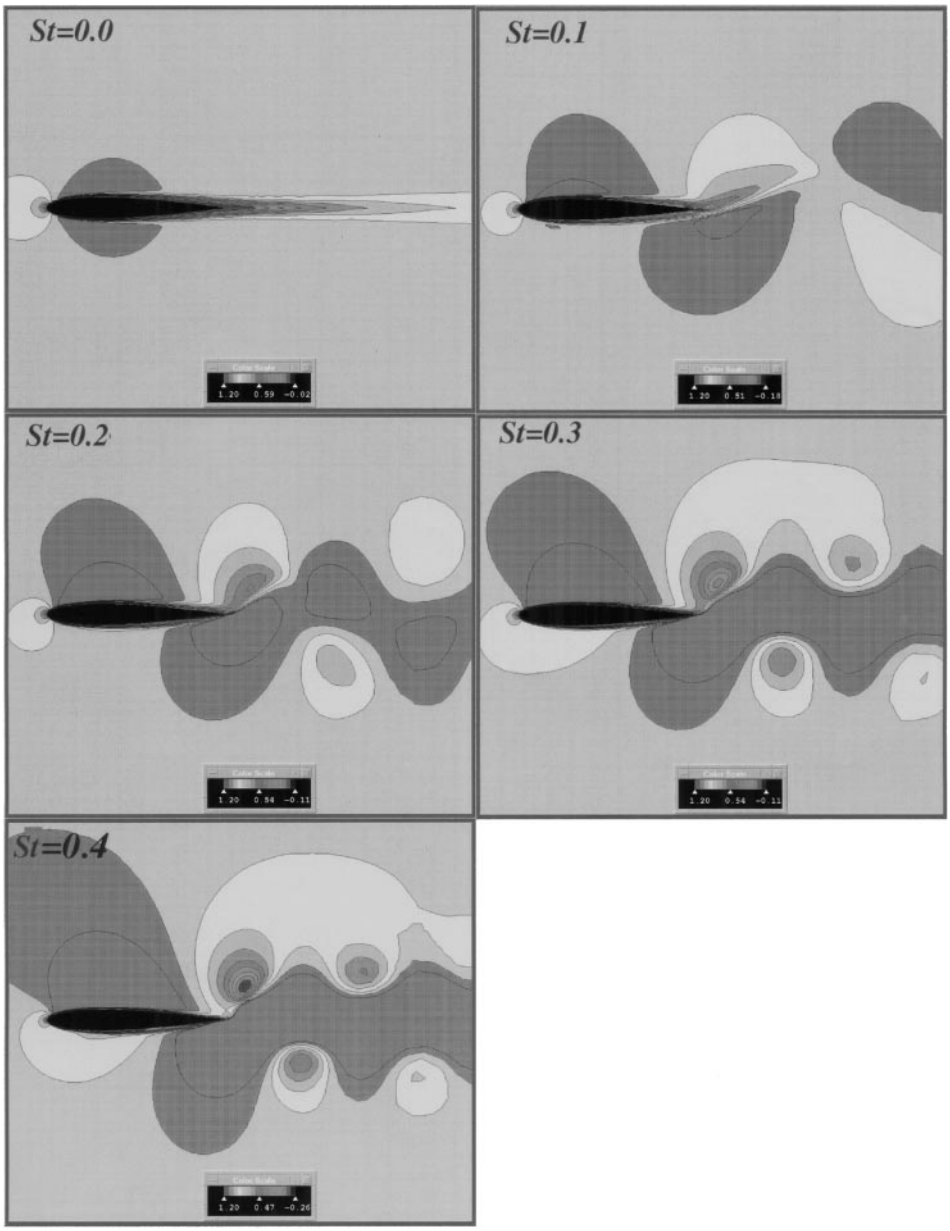

FIG. 7. Iso-velocity contours around an oscillating airfoil NACA0012. (Re = 7200.)

agreement with the experimental results by Triantafyllou *et al.* [9] although their airfoil was in a different mode of pitching and heaving motion. This optimal phenomenon of thrust generation can be explained by the visualized velocity contours against the reduced frequencies around the pitching airfoil as illustrated in Fig. 7. The thrust generation, when the Strouhal number St is larger than 0.1, corresponds to a staggered array of the reverse von Karman vortices in the wake and an intense accelerated fluid, the jet stream in the center, which generates a forward force, i.e., the thrust. Then, an increase in the Strouhal number leads to more vortex shedding from the trailing edge even though the more the jet stream

strengthens and widens, the more energy is dissipated into the wake through the vortex shedding. Hence, the thrust increases (Figs. 6a and 6b) with increasing Strouhal number (or reduced frequency) but the propulsive efficiency reaches a peak at some point between 0.25 and 0.35.

Note that the propulsive efficiencies of oscillating foils show rather lower values than those achieved as expected by undulatory swimming fishes. One may expect that parameters like amplitude and pivot point and other motion like heaving might influence the performance of the jet-stream propulsion. However, as can be seen in the following section, an optimal relationship should exist between the mode of motion and the geometry of the oscillating body in the performance of the jet-stream propulsion, and the undulatory swimming of aquatic animals is an excellent example of this.

Hydrodynamics and the Mechanism of Undulatory Swimming

A grid system of 199 streamwise grids, 41 grids in the direction vertical to the body surface, and 50 grids in the wake was employed in the present simulation. The minimum grid spacing adjacent to the body surface was controlled with an experiential formula of $\delta_\zeta = 0.1/\sqrt{\mathrm{Re}} \approx 0.001$. Grids were clustered at the solid wall to resolve viscous flow inside the boundary layer as well as at the leading and trailing edges because of the steep pressure divergence. The computational domain was limited to a region around the body with a radius for the outside open boundary of six body lengths. The reduced frequency of 5.843 leads to a nondimensionalized period of approximately 0.54 and a time increment dt of 0.005 was taken. The computation was carried out for nine stroke cycles, using an HP Apollo 9000 series workstation (Model 755).

Hydrodynamics during a Stroke Cycle

Figures 8a–8d illustrate the iso-velocity surfaces behind the undulatory swimming tadpole and the iso-velocity contours on the horizontal symmetrical middle plane at four moments of $0/T$, $T/8$, $2T/8$, and $3T/8$ in a quarter stroke cycle. It is clearly seen that, for all moments of a stroke cycle, a staggered array of the reverse von Karman vortices (colored green) is detected in the wake, forming an intense accelerated fluid (colored red), i.e., the jet stream backward in the center, which generates an opposite force to thrust the body forward. The vortices are quite 3D in structure, in particular at the tail tip, with a width roughly equal to the greatest amplitude of the tail tip ($0.2L$) in the stroke plane (the symmetrical middle plane) and a height equivalent to the greatest height of the tail. The vortex structure in the wake is a result of shedding of vortices from both sides of the plate-like tail. The vortices are initiated by the shear flow over the tail fin, starting just caudal to the base of the tail. They grow down the tail and are shed at the tail tip into the wake. Additionally, the velocity gradient over the dorsal fin of the tail results in a pair of small longitudinal vortices down the tail tip. An overview of the streamlines flowing over the undulating tadpole, as shown in Figs. 9a and 9b, however, reveals that these longitudinal vortices merely lead to the freestreamwise flow spiraling down the tail to be shed into the wake. The wake patterns are qualitatively similar to the above 2D results of the oscillating airfoil and closely match the wake visualized behind a robotic tuna by Triantafyllou and Triantafyllou [12]. Characteristic of the unique shape of tadpoles, a pair of vortices is also detected at the end of the head and the tail, forming a low-velocity region, namely, the “dead water” zone, due to the abrupt transition

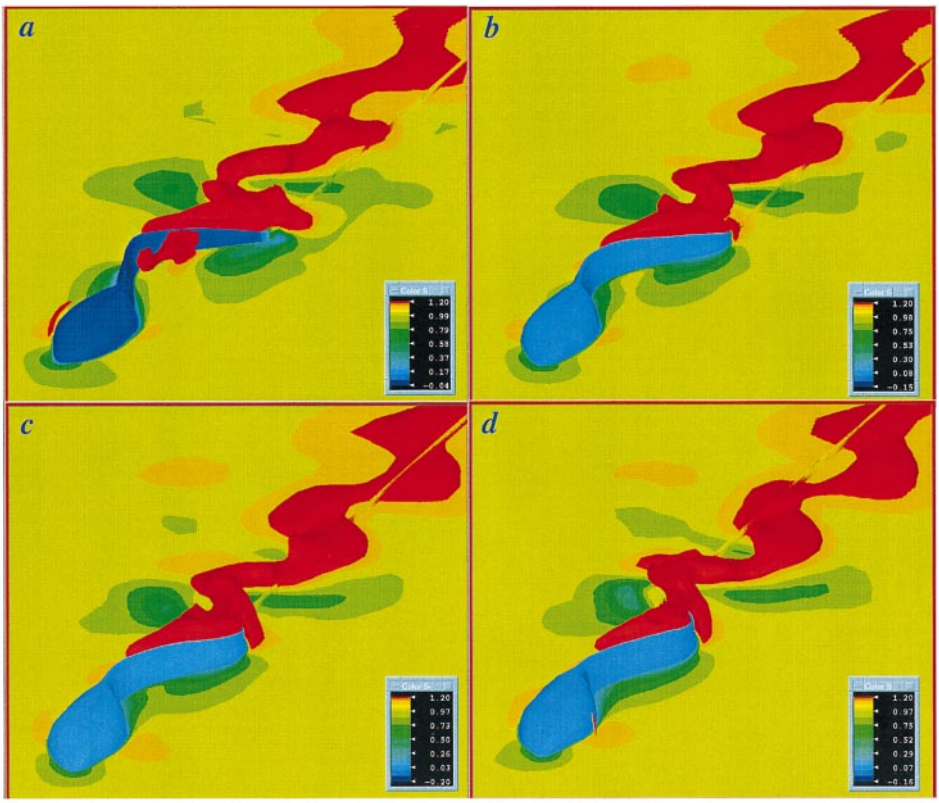

FIG. 8. Iso-velocity surfaces around an undulatory swimming tadpole-shaped body at (a) $t/T = 0$; (b) $t/T = 1/8$; (c) $t/T = 2/8$; and (d) $t/T = 3/8$. ($\mathrm{Re} = 7200$, $k = 5.843$.)

from the globose body. This special region, however, located immediately after the moment center of tadpoles, barely influences their propulsive performance [15].

Figures 9a and 9b show the instantaneous streamlines around the tadpole, the iso-pressure contours on the body surface, and the top view of velocity vectors at two instants when the head–body of the tadpole forms a C- and S-configuration [15]. These figures show roughly similar pressure distributions and flow patterns in the symmetrical middle plane, compared with our previous 2D study (Fig. 6A and Fig. 6B in Liu *et al.* [15]) correspondingly. The C-configuration (Fig. 9a) corresponds to the maximum thrust, when the tail takes an arched form with a maximum angle of incidence, i.e., the angle of attack with a maximum area to push the fluid backward. The instantaneous angle of attack was calculated using the first derivative of Eq. (15) to be approximately 56°, much greater than the stall angle of about 10° in the steady case. This means that the aquatic animals undergoing undulatory swimming very likely utilize the phenomenon of dynamic stall to efficiently generate the dynamic vorticial flow and the jet stream. The iso-pressure contours further show that both sides of the C-shaped tail (Fig. 9a), pushed by the positive pressure region (colored orange) or sucked by the negative pressure (colored blue), contribute to thrust generation. Correspondingly, the drag due to skin friction reaches a minimum, which implies that the undulatory swimmer can achieve the best performance at the moment. On the other hand, focusing on the streamlines around the body, it is seen that the flow is 3D in structure, with strong secondary flow (cross flow) at the snout and at the edges of the dorsal and

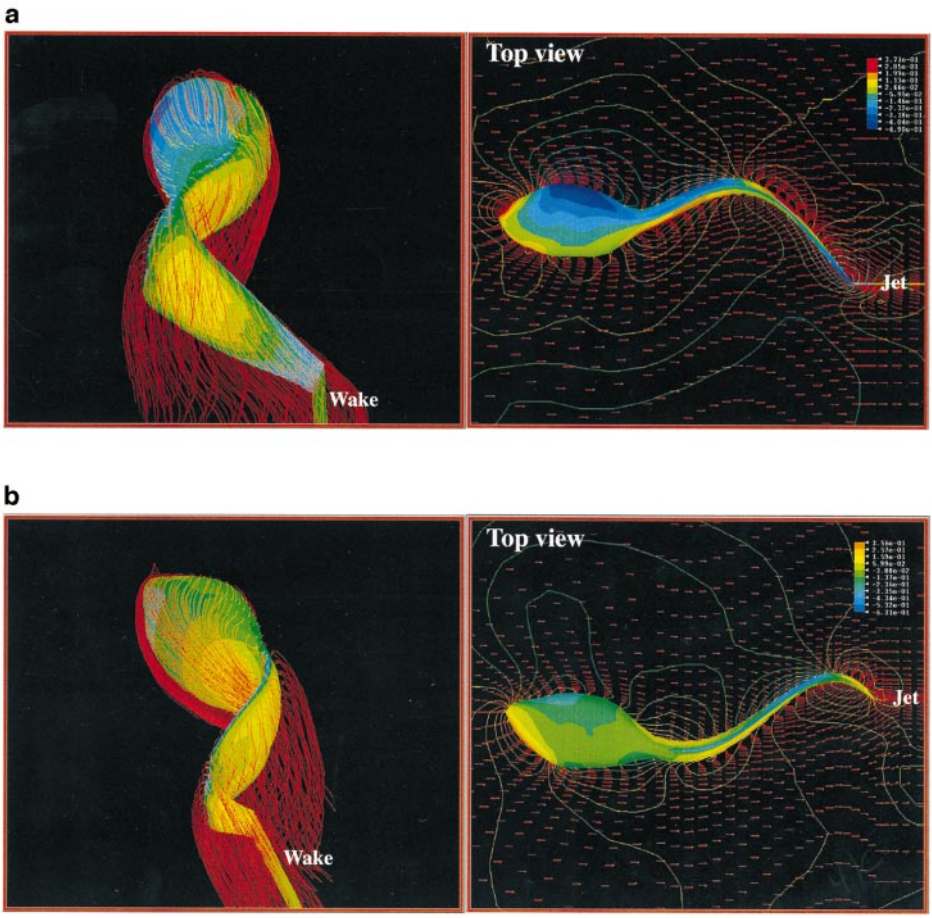

FIG. 9. Instantaneous streamlines around an undulatory swimming tadpole-shaped body with body surface covered by pressure contours and velocity vectors and iso-pressure contours in the symmetrical middle plane when the tadpole tail forms: (a) C-configuration and (b) S-configuration. (Re = 7200, $k = 5.843$.)

ventral tail fin. The streamlines and the pressure distribution over a large portion of the tail appear in general quite two-dimensional, with little vertical cross flow over most of the tail, except within a small region limited to the dorsal and ventral tail fin. This shows evidence of the theoretical results of Cheng *et al.* [7] based on the 3D waving plate theory, wherein undulatory motion can produce three-dimensional effects.

Triantafyllou *et al.* [9] reported that most fishes swim within a narrow region of the Strouhal number ranging over 0.25–035. The calculated Strouhal number for the tadpole, however, yields a value of 0.72, approximately twice those observed in fishes [9]. A comparison of tail-beat frequency versus specific swimming speed among fishes and tadpoles [16] shows a tight regression line for tadpoles and fishes. Hence, the higher tail amplitude (almost double that of carangiform fish such as salmon and trout), as a result, contributes to the higher Strouhal number for tadpoles. This reveals that tadpoles manage to swim efficiently in comparison with fishes, but using a different mode.

As illustrated in Figs. 9a and 9b, the flow shows quite strong 3D structure, i.e., cross flow, over the head–body, leading to a very strong girthwise (crosswise) pressure gradient.

However, in contrast to what generally occurs with steady flow, a longitudinal pressure gradient, namely the so-called leading-edge suction region [2–4] at the snout, is barely detectable during the whole undulating cycle. This is because the idea of the leading-edge suction region was based on the case of steady flow around a "streamlined" fish, without accounting for any lateral oscillation of the snout. However, the present analysis shows that the suction region does exist, but it alternates laterally from side to side in the undulating tadpole. We believe that the large-amplitude ($\max = 0.05L$) lateral motion of the tadpole's snout is more likely to push or suck the incoming flow to either side of the snout rather than toward its upper or lower surfaces. This can be further confirmed by the visualized flow in the side view at the instant when the tail is in the C-configuration position (Fig. 9a). A large suction region, with a lower pressure "island" (shown in blue in Fig. 9a), is detected on the left side, which is quite 3D in structure. A high-pressure region is also detected on the corresponding right side. However, the local inclination of the pressure at the snout, i.e., the suction, would not seem large enough for this low-pressure region to contribute much to forward force (i.e., thrust).

Additionally, it is obvious that the lateral oscillation of the undulating tadpole, as seen in Figs. 9a and 9b, leads to a very large pressure difference across the snout. This result strongly supports the analysis by Lighthill [23] that pure sideslip of the heads of clupeid fish would generate a great pressure difference, but simultaneous yawing could enormously reduce the effective pressure difference and any associated cross-flow effects. Also, the cross flow that we observed changed significantly with each instant in the stroke cycle (see2 Figs. 9a and 9b). This further implies that limiting this cross flow, as pointed out by Lighthill [23], with appropriate simultaneous yawing, should reduce the resistance during undulatory swimming.

Performance of the Jet-Stream Propulsion

The time variations of the thrust coefficient (C_T), power coefficient (C_P), and drag coefficient (C_D) due to friction were plotted against time in a nondimensionalized manner in Fig. 10. The mean thrust (see Appendix I) due to the pressure normal to the surface is readily produced during the whole stroke cycle and the sum of the thrust coefficient and

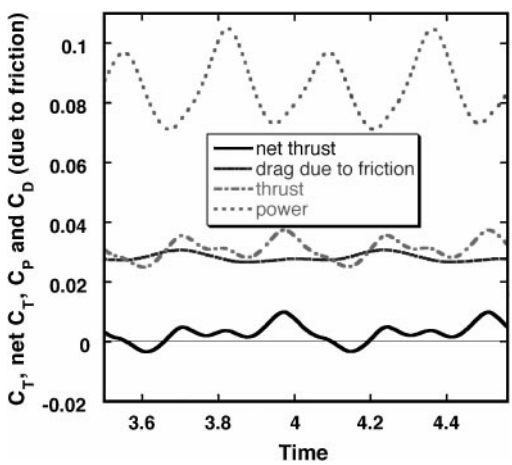

FIG. 10. Time variation of instantaneous thrust (C_T), power coefficients (C_P), and drag due to friction (C_D). (Re = 7200, $k = 5.843$.)

drag coefficient, i.e., the net thrust coefficient, now has a very small mean magnitude of 0.01. Since the undulating tadpole model is forced (restrained) to swim in a stream with constant velocity at a given Re, zero net thrust (i.e., sum of thrust and drag coefficients), therefore, indicates trimmed swimming. The drag due to skin friction shows slight fluctuation, unlike the distinct periodicity seen for drag in the previous 2D analyses [15], where the periodicity was thought to be due to the large region of flow separation, whose magnitude changed with time, as well as to the unsteady boundary layer. Here the reduced fluctuations in drag are the key reason that the "dead water" zone at the base of the tail and the unsteady boundary layer over the tail are 3D in structure. Additionally, the friction drag in general, as a price for producing the pressure-based thrust, shows a significant increase with velocity gradient enhancement by the oscillating surface (Figs. 8a–8d), in particular over most of the tail. This is confirmed by the fact that the friction drag coefficient during undulatory swimming, calculated as 0.030, is approximately 2.5 times greater than that in the steady case of straight tail-fixed tadpole swimming (0.0118). This means that using the dead drag in calculating the force-related quantities concerning an undulatory swimming object would seriously underpredict the real drag produced [24].

Following the method as defined in Eq. (19), which uses the mean thrust multiplied by the forward swimming speed divided by the required power, we obtained a mean propulsive efficiency (η) of about 0.45. This value is much higher, by approximately 50%, than those achieved by the 2D oscillating airfoils. As mentioned above, undulatory swimming can achieve a much better performance than a rigidly oscillating mode of motion. For comparison, the propulsive efficiency was also calculated by using conventional elongated-body theory without [25] and with [7] the slope effect at the tail tip. If just the hydrodynamic force associated with the vortex sheet from the tail in the absence of any vortex shedding from the body fins [4] is considered and if the propagating wave is defined by Eq. (13) then, according to the elongated-body theory of Lighthill [25], the propulsive efficiency is

$$\eta = \frac{1}{2}(1+\beta) - \frac{1}{2}\alpha^2\frac{\beta^2}{1+\beta}, \qquad \beta = \frac{U}{V}, \qquad \alpha = \frac{\lambda}{2\pi}\frac{h'(L)}{h(L)}, \tag{22}$$

where $V = f\lambda$ denotes the wave speed and $h'(L)$ is the local slope at the tail tip, which obviously influences the propulsive efficiency. Lighthill [26] suggested that to make the propulsive efficiency close to unity, it is desirable for this $h'(L)$ to be practically zero because a nonzero value of $h'(L)$ reduces the thrust without altering the power. However, like some aquatic animals tadpoles do not utilize a constant-amplitude envelope near the caudal tail tip (Fig. 3). Following Cheng *et al.* [7], here the effect of the slope at the tail tip was also considered in the calculation of the propulsive efficiency. Given the kinematic data in the section the kinematic model and the slope calculated based on the amplitude–body length curve in Fig. 3, the propulsive efficiency without the slope term was evaluated to be 0.83 and that with the slope term was 0.70.

CONCLUDING REMARKS

A feasible modeling of undulatory locomotion at moderate Reynolds numbers has been made on the basis of a time-dependent solution of the Navier–Stokes equations, of an unsteady, viscous, dynamic vortex flow field around an undulatory swimmer that can undergo arbitrary, large-amplitude movements of realistic undulatory swimming. Successfully modeling the unsteady hydrodynamics of a realistic three-dimensional tadpole-shaped

model has thereby established the importance of accurately predicting a staggered array of reverse von Karman vortices, the jet stream, and their correlation with thrust generation. The present results also point to an optimal propulsive mechanism appropriate to undulatory swimming, which is achieved by a best coupling of the geometry and the motion matched to the body.

APPENDIX I: NOMENCLATURE

x, y, z	Boxy-fixed Cartesian coordinates
ξ, η, ζ	Body-fitted coordinates
t	Physical time
Δt	Physical time increment
τ	Pseudo time
$\Delta\tau$	Pseudo time increment
Re	Reynolds number
St	Strouhal number
ν_t	Eddy viscosity
$\mathbf{u}_0$	Velocity of swimmer
$\mathbf{a}_0$	Acceleration (or deceleration) of swimmer
$V(t)$	Volume of control volume
V_{ijk}	Volume at cell (i, j, k)
$\Delta V_{ijk}^{(n)}$	Increment of the volume at cell (i, j, k) at time step (n)
$S(t)$	Surface of the control volume
i, j, k	Cell index
(n)	Physical time iteration number
(m)	Inner iteration number
$k = 2\pi f c_m / 2U_{\text{ref}}$	Reduced frequency
f	Pitching frequency
L	Tadpole body length (reference length)
S_w	Surface area of the tadpole
ρ	Water density
$C_{\text{T}} = \frac{\text{Thrust}}{\frac{1}{2}\rho U^2 S_{\text{body}}}$	Thrust coefficient
$C_{\text{P}} = \frac{\text{Power}}{\frac{1}{2}\rho U^3 S_{\text{body}}}$	Power coefficient
$C_{\text{D}} = \frac{\text{Drag}_{\text{friction}}}{\frac{1}{2}\rho U^2 S_{\text{body}}}$	Drag coefficient due to skin friction

APPENDIX II: EVALUATION OF INVISCID FLUX

Following Roe's flux-differencing splitting [27], the inviscid flux vector at $i \pm \frac{1}{2}$ is defined for the one-dimensional case as

$$\hat{\mathbf{F}}_{i\pm1/2} = \hat{\mathbf{F}}\left(\mathbf{q}^{\text{LR}}_{i\pm1/2}\, \mathbf{S}^{\xi}_{i\pm1/2}\right) \pm \mathbf{A}^{\pm}_{i\pm1/2}\delta\mathbf{q}^{\text{LR}}_{i\pm1/2}, \tag{AII.1}$$

where

$$\delta\mathbf{q}^{\text{LR}}_{i\pm1/2} = \mathbf{q}^{\text{R}}_{i\pm1/2} - \mathbf{q}^{\text{L}}_{i\pm1/2}, \qquad \begin{aligned} \mathbf{q}^{\text{R}}_{i+1/2} &= \mathbf{q}_i + (1-\phi_2)\delta\mathbf{q}_{i+1/2} - \phi_1\delta\mathbf{q}_{i+3/2} \\ \mathbf{q}^{\text{L}}_{i+1/2} &= \mathbf{q}_i + \phi_1\delta\mathbf{q}_{i-1/2} + \phi_2\delta\mathbf{q}_{i+1/2}. \end{aligned} \tag{AII.2}$$

Superscripts R and L denote the left and right sides of the reconstructed flux vector corresponding to the interface between the two adjacent cells in a MUSCL [28] manner. The matrix $\mathbf{A}^{\pm}_{i\pm1/2}$ is constructed from the local velocity components and the metrics and is then reconstructed based on the eigenvalue decomposition analysis. The second term in which $\mathbf{q}^{\mathrm{R}}_{i\pm1/2}$ and $\mathbf{q}^{\mathrm{L}}_{i\pm1/2}$ appear can be interpolated using the flow variables from the adjacent cell centers. Implementation of different order schemes can be realized by selecting the appropriate values for the parameters ϕ_1 and ϕ_2. In this work, the third-order upwind scheme when $\phi_1 = 1/6$ and $\phi_2 = 1/3$ is used to ensure the accuracy of the evaluation of the RHS, while the first-order scheme is used for the LHS, where $\phi_1 = \phi_2 = 0$.

The Jacobian matrix $\mathbf{A}^{\pm}_{i\pm1/2}$ may be reformed as

$$\mathbf{A}^{\pm} = \mathbf{A}^{\mathrm{R}} \Lambda^{\pm} \mathbf{A}^{\mathrm{L}}, \tag{AII.3}$$

where the two matrices $\mathbf{A}^{\mathrm{R}}$ and $\mathbf{A}^{\mathrm{L}}$ are reconstructed from the eigenvalue decomposition of the inviscid Jacobian matrix $\mathbf{A}$, which is initially built using the flow variables at the interface of the cells and the following metrics of

$$\mathbf{A}^{\pm}_{i+1/2} = \mathbf{A}\left(\mathbf{q}^{\mathrm{LR}}_{i\pm1/2}, \mathbf{S}^{\xi}_{n_{i\pm1/2}}\right) = \mathbf{S}\begin{bmatrix} \bar{\mathbf{U}}\delta_{lm} + \mathbf{U}_l n_m & n_l \\ \beta n_m & 0 \end{bmatrix}, \qquad l, m = 1, 2, 3, \tag{AII.4}$$

where $\mathbf{U} = 0.5(\mathbf{q}^{\mathrm{L}}_{i\pm1/2} + \mathbf{q}^{\mathrm{R}}_{i\pm1/2}) - \mathbf{u}_g$, $\bar{\mathbf{U}} = \mathbf{U} \cdot \mathbf{n}$. Note that the first-order scheme $\mathbf{q}^{\mathrm{LR}}_{i\pm1/2}$ is chosen for the LHS and a third-order scheme is used for the RHS. The diagonal matrix $\Lambda^{\pm}$ is given as

$$\begin{gathered} \Lambda^{\pm} = \mathrm{diag}[\lambda^{\pm}_1, \lambda^{\pm}_2, \lambda^{\pm}_3, \lambda^{\pm}_4], \qquad \lambda^{\pm}_m = \frac{\lambda_m \pm |\lambda_m|}{2}, \qquad \lambda_1 = \lambda_2 = \mathbf{S}\bar{\mathbf{U}}, \\ \lambda_3 = \mathbf{S}(\bar{\mathbf{U}} + \mathbf{c}), \qquad \lambda_4 = \mathbf{S}(\bar{\mathbf{U}} - \mathbf{c}), \qquad \mathbf{c} = \sqrt{\mathbf{U}^2 + \beta}, \end{gathered} \tag{AII.5}$$

where $\mathbf{c}$ denotes the speed of sound.

At the solid wall stencils where $k = 1$, utilization of the boundary-fitted grid system leads to a zero contravariant velocity $\mathbf{U}$ for the LHS and the eigenvalue $\lambda_3 = \mathbf{Sc}$, while the other three components are zero. Hence, the array $\mathbf{C}^{+}_{k-1/2}$ at $k - 1/2$ for the LHS can be simply given as

$$\mathbf{C}^{+}_{k-1/2} = \frac{\mathbf{S}}{2}\begin{bmatrix} n_l n_m \mathbf{c} & n_l \\ \beta n_m & \mathbf{c} \end{bmatrix}, \qquad l, m = 1, 2, 3, \tag{AII.6}$$

where the speed of sound $\mathbf{c} = \sqrt{\beta}$.

For the RHS, the term $\hat{\mathbf{H}}_{k-1/2}$ at $k - 1/2$ when $k = 1$ is given as

$$\hat{\mathbf{H}}_{k-1/2} = \begin{bmatrix} 0 & \mathbf{S}n_l \\ \beta n_m & 0 \end{bmatrix}\begin{bmatrix} \mathbf{u}_{\mathrm{sw}} \\ p_{\mathrm{sw}} \end{bmatrix}, \qquad l, m = 1, 2, 3, \tag{AII.7}$$

where $\mathbf{u}_{\mathrm{sw}}$ is the local velocity of the solid wall, and p_{sw} is the pressure on the solid wall.

Based on Eq. (AII.1), the inviscid-related part of the term $\Delta\mathbf{R}_{ijk}^{(n,m)}$ in Eq. (14) can be linearized, by introducing the first-order scheme for the LHS, to become

$$\begin{aligned}\mathbf{R}_{ijk}^{(\text{inviscid})} &= \mathbf{A}^-_{i+1/2}\mathbf{q}_{i+1} + (\mathbf{A}^+_{i-1/2} - \mathbf{A}^-_{i+1/2})\mathbf{q}_i - \mathbf{A}^+_{i-1/2}\mathbf{q}_{i-1} + \mathbf{B}^-_{j+1/2}\mathbf{q}_{j+1} \\ &\quad + (\mathbf{B}^+_{j-1/2} - \mathbf{B}^-_{j+1/2})\mathbf{q}_j - \mathbf{B}^+_{j-1/2}\mathbf{q}_{j-1} + \mathbf{C}^-_{k+1/2}\mathbf{q}_{k+1} \\ &\quad + (\mathbf{C}^+_{k-1/2} - \mathbf{C}^-_{k+1/2})\mathbf{q}_k - \mathbf{C}^+_{k-1/2}\mathbf{q}_{k-1}. \end{aligned} \tag{AII.8}$$

Matrices **B** and **C** are constructed in a manner similar to matrix **A**. In the preceding equation, terms such as $\hat{\mathbf{F}}(\mathbf{q}^{\text{LR}}_{i\pm1/2}, \mathbf{S}^{\xi}_{i\pm1/2})$ in three directions cancel out completely when the first-order upwind scheme is implemented. For the right hand side of Eq. (14), a third-order upwind scheme is used to ensure the accuracy of the evaluation of the RHS at each time step, which involves the calculation of terms like $\hat{\mathbf{F}}(\mathbf{q}^{\text{LR}}_{i\pm1/2}, \mathbf{S}^{\xi}_{i\pm1/2})$.

APPENDIX III: EVALUATION OF VISCOUS FLUX

The viscous fluxes are obtained from the application of Gauss's theorem to each cell, where the velocity derivatives of the cell centroid with respect to x, y, and z are approximated by the discrete integral over the cell faces. Taking, for example, the one-dimensional case

$$\int_{V_{i+1/2}} u_x \, dx\, dy\, dz = V_{i+1/2} u_{xi+1/2}, \tag{AIII.1}$$

where the discretized integral is calculated at six faces of the structured cell, i.e., a tetrahedron, across the two adjacent cells of (i, j, k) and $(i+1, j, k)$, resulting in a second-order center differencing scheme. The final, linearized form of the viscous fluxes for both the LHS and RHS becomes

$$\begin{aligned}&\mathbf{R}_{ijk}^{(\text{viscous})} \\ &= \left(\frac{\partial \hat{\mathbf{F}}_v}{\partial \mathbf{q}^+}\right)_{i+1/2}\mathbf{q}_{i+1} + \left[\left(\frac{\partial \hat{\mathbf{F}}_v}{\partial \mathbf{q}^+}\right)_{i+1/2} - \left(\frac{\partial \hat{\mathbf{F}}_v}{\partial \mathbf{q}^+}\right)_{i-1/2}\right]\mathbf{q}_i + \left(\frac{\partial \hat{\mathbf{F}}_v}{\partial \mathbf{q}^+}\right)_{i-1/2}\mathbf{q}_{i-1} \\ &\quad + \left(\frac{\partial \hat{\mathbf{G}}_v}{\partial \mathbf{q}^+}\right)_{j+1/2}\mathbf{q}_{j+1} + \left[\left(\frac{\partial \hat{\mathbf{G}}_v}{\partial \mathbf{q}^+}\right)_{j+1/2} - \left(\frac{\partial \hat{\mathbf{G}}_v}{\partial \mathbf{q}^+}\right)_{j-1/2}\right]\mathbf{q}_j + \left(\frac{\partial \hat{\mathbf{G}}_v}{\partial \mathbf{q}^+}\right)_{j-1/2}\mathbf{q}_{j-1} \\ &\quad + \left(\frac{\partial \hat{\mathbf{H}}_v}{\partial \mathbf{q}^+}\right)_{k+1/2}\mathbf{q}_{k+1} + \left[\left(\frac{\partial \hat{\mathbf{H}}_v}{\partial \mathbf{q}^+}\right)_{k+1/2} - \left(\frac{\partial \hat{\mathbf{H}}_v}{\partial \mathbf{q}^+}\right)_{k-1/2}\right]\mathbf{q}_k + \left(\frac{\partial \hat{\mathbf{H}}_v}{\partial \mathbf{q}^+}\right)_{k-1/2}\mathbf{q}_{k-1} \\ &\quad + \hat{\mathbf{F}}^*_{vi+1/2} - \hat{\mathbf{F}}^*_{vi-1/2} + \hat{\mathbf{G}}^*_{vj+1/2} - \hat{\mathbf{G}}^*_{vj-1/2} + \hat{\mathbf{H}}^*_{vk+1/2} - \hat{\mathbf{H}}^*_{vk-1/2}, \end{aligned} \tag{AIII.2}$$

where the first nine terms express the linearized part and the last six terms are the off-diagonal elements that will be moved to the RHS.

The viscous Jacobian $(\partial \hat{\mathbf{F}}_v / \partial \mathbf{q}^{\pm})_{i+1/2}$ in the i-sweep, for instance, is

$$\left(\frac{\partial \hat{\mathbf{F}}_v}{\partial \mathbf{q}^{\pm}}\right)_{i+1/2} = -\frac{1}{V_{i+1/2}}\left(\frac{1}{\text{Re}} + \nu_t\right)\begin{bmatrix} \left(\mathbf{S}^{\xi}_n\right)_m f_l + \delta_{lm}\mathbf{S}^{\xi}_n \cdot \mathbf{f} & 0 \\ 0 & 0 \end{bmatrix}, \qquad l, m = 1, 2, 3, \tag{AIII.3}$$

where $V_{i+1/2}$ denotes the volume of a cell constructed at the cell interface; $\mathbf{f} = (f_1, f_2, f_3)$ is represented by the surface areas of the cell; and subscripts l and m denote 1, 2, and 3, which correspond to x, y, and z. Special modifications are made at the solid wall stencils in constructing the matrix $\hat{\mathbf{H}}_{vk-1/2}$ where $k = 1$, accounting for the local velocity of the moving wall.

APPENDIX IV: GRID GENERATION ON THE BODY SURFACE AND IN THE DOMAIN

Grids are first generated on the body surface. Initial grids at cross sections in the longitudinal direction are further redistributed to up to one hundred cross sections with sufficient small, uniform grid spacing. On demand for grid number, grid spacing, clustering rate, and so forth, two ξ grid lines on the two curves of L_1 and L_2 and two η grid lines on the curve L_1 at the snout and the tail tip are formed in advance. For an η grid line on the body surface as illustrated in Fig. 4b, grids are generated on the grid line analytically. The following procedure is implemented: (1) determine the right and left cross sections by the given two points at two ends of the designated grid line; (2) divide the grid line in the longitudinal direction with uniform spacing

$$dx = (x_R - x_L)/(jm - 1) \qquad \text{and} \qquad x_j = x_L + dx(j - 1), \tag{AIV.1}$$

and in the chordwise direction with a uniform angle increment

$$\delta\alpha = \pi/2(jm - 1) \qquad \text{and} \qquad \alpha j = \delta\alpha(j - 1); \tag{AIV.2}$$

(3) interpolate the cross section at the given x_j to determine the elliptic curve with two axes a_j and b_j; and (4) give the coordinates y_j and z_j at the point j by

$$y_j = a_j \cos(\alpha j) \qquad \text{and} \qquad z_j = b_j \sin(\alpha j). \tag{AIV.3}$$

The grid line is further clustered similarly to those on the two curves. On the other hand, the grid lines ξ eventually yield connecting grid points on each η grid line.

The open boundary as shown in Fig. 5 is defined by using a quarter-sphere with radius R for block I covering the head–body and a circular cylinder with the same radius R for block II and block III covering the tail and wake. Grids on the open boundary of block I are uniformly generated. Grids on the open boundary for blocks II and III are made having the same rate of grid clustering and grid spacing as those on the body surface and in the wake such that the quality of the grids can be maintained during regridding.

Grids in the domain are then generated by using an algebraic method [29] in each block. Note that the configuration at the tail tip is slightly modified as illustrated in Fig. 5 to end with a nonzero height fin instead of tapering to one point, in order to ensure quality of grids when regridding. Thus, minor modification of the tail tip geometry was made (see Fig. 1b) and verified to barely affect the flow in both the steady and unsteady simulations. According to the form of traveling wave which is a function of longitudinal position as shown in Eq. (15), grid lines at the tail tip and in the wake, therefore, remain nearly straight during regridding, merely stroking side by side at each section, which significantly enhances both the stability and the speed of convergence.

Regridding at each time step is performed by first moving grids vertically side by side on the body surface according to the undulating mode of Eq. (15) without any stretching

(movement) in the longitudinal direction under the assumption of body elongation during swimming. Grids on the cut plane in the wake are forced to move with the same distance as that on the grid line at the tail tip. Grids in the domain are regenerated as

$$y(i, j, k)^{(n)} = y(i, j, k)^{(0)} + dy(i, j, 1)^{(\text{body})}, \tag{AIV.4}$$

where coordinate y at grid (i, j, k) of a time level n is updated by adding an increment of vertical movement of $y(i, j, 1)^{(\text{body})}$ on the body surface to the initial $y(i, j, k)^{(0)}$, whereas coordinates x and z remain unchanged. Implementation of the previous regridding process is capable of maintaining the quality of the initial grids as well as reducing the regridding to a minimized level.

ACKNOWLEDGMENTS

This research was sponsored by the Japan Science and Technology Corporation. Special thanks go to Dr. Richard Wassersug for his continuous support during the present project.

REFERENCES

1. M. J. Lighthill, *Annu. Rev. Fluid Mech.* **1**, 413 (1969).
2. T. Y. Wu, Hydrodynamics of swimming propulsion. Part 1. Swimming of a two-dimensional flexible plate at variable forward speeds in an inviscid fluid, *J. Fluid Mech.* **46**, No. 2, 337 (1971).
3. T. Y. Wu, Hydrodynamics of swimming propulsion. Part 2. Some optimal shape problems, *J. Fluid Mech.* **46**, No. 3, 521 (1971).
4. T. Y. Wu, Hydrodynamics of swimming propulsion. Part 3. Swimming and optimum movements of slender fish with side fins, *J. Fluid Mech.* **46**, No. 3, 545 (1971).
5. J. N. Newman, The force on a slender fish-like body, *J. Fluid Mech.* **58**, No. 4, 689 (1973).
6. M. J. Lighthill, Large-amplitude enlongated-body theory of fish locomotion, *Proc. R. Soc. B* **179**, 125 (1972).
7. J. Y. Cheng, L. X. Zhuang, and B. G. Tong, Analysis of swimming three-dimensional waving plates, *J. Fluid Mech.* **232**, 341 (1991).
8. M. M. Koochesfahani, Vortical patterns in the wake of an oscillating airfoil, *AIAA J.* **27**, No. 9, 1200 (1989).
9. G. S. Triantafyllou, M. S. Triantafyllou, and M. A. Grosenbaugh, Optimal thrust development in oscillating foils with application to fish propulsion, *J. Fluid Struct.* **7**, 205 (1993).
10. K. Streilien, G. S. Triantafyllou, and M. S. Triantafyllou, *AIAA J.* **34**, No. 11, 2315 (1996).
11. J. M. Anderson, K. Streitlien, D. S. Barrett, and M. S. Triantafyllou, *J. Fluid. Mech.* **360**, 1 (1998).
12. M. S. Triantafyllou and G. S. Triantafyllou, An efficient swimming machine, *Sci. Am.* **3**, 1 (1995).
13. H. Liu, S. Sunada, and K. Kawachi, Unsteady solutions to the incompressible Navier–Stokes equations with the pseudo-compressibility method, *in* ASME publications, Fluids Engineering Division, Vol. 215, p. 105, 1995.
14. H. Liu, A numerical study of jet-stream propulsion of oscillating bodies, *J. Soc. Naval Architects Jpn.* **178**, 101 (1995).
15. H. Liu, R. Wassersug, and K. Kawachi, A computational fluid dynamic study of tadpole swimming, *J. Exp. Biol.*, **199**, No. 6, 1024 (1996).
16. R. Wassersug and K. Hoff, The kinematics of swimming in anuran larvae, *J. Exp. Biol.* **119**, 1 (1985).
17. J. J. Videler, *Fish Swimming* (Chapman & Hall, London, 1993).
18. P. D. Thomas and C. K. Lombard, Geometric conservation law and its application to flow computation on moving grids, *AIAA J.* **17**, No. 10, 1030 (1979).
19. R. M. Beam and R. F. Warming, An implicit factored scheme for the compressible Navier–Stokes equations, *AIAA J.* **15**, No. 4, 393 (1978).

20. S. E. Roger, D. Kwak, and C. Kiris, Steady and unsteady solutions of the incompressible Navier–Stokes equations, *AIAA J.* **29**, No. 4, 1603 (1991).
21. H. Liu and K. Kawachi, A numerical study of insect flight, *J. Comput. Phys.* **146**, No. 1, 124 (1998).
22. T. Von Karman and J. M. Burgers, General aerodynamic theory-perfect fluids, in *Aerodynamic Theory*, edited by W. F. Durand, Division E, Vol. II (1943), p. 308.
23. M. J. Lighthill, Estimates of pressure differences across the head of a swimming clupeid fish, *Philos. Trans. R. Soc. London B* **341**, 129 (1993).
24. P. W. Webb, Hydrodynamics and energetics of fish propulsion, *Bull. Fish. Res. Bd. Can.* **190**, 1 (1975).
25. M. J. Lighthill, *Mathematical Biofluiddynamics* (SIAM, Philadelphia, 1975).
26. M. J. Lighthill, Note on the swimming of slender fish, *J. Fluid. Mech.* **9**, 305 (1960).
27. P. Roe, Approximate Riemann solvers, parameter vectors and difference scheme, *J. Comput. Phys.* **43**, No. 2, 357 (1981).
28. B. Van Leer, Toward the ultimate conservative differencing scheme. 4. A new approach to numerical convection, *J. Comput. Phys.* **23**, 276 (1977).
29. L. E. Eeiksson, Generation of boundary-conforming grids around wing-body configurations using transfinite interpolation, *AIAA J.* **20**, No. 10, 1313 (1982).